ARTICLES
https://doi.org/10.1038/s41566-022-00971-7

nature photonics

Electrically controllable chirality in a nanophotonic interface with a two-dimensional semiconductor

Robert Shreiner[1,2,4], Kai Hao[1,4], Amy Butcher[1] and Alexander A. High[1,3] ✉

Chiral nanophotonic interfaces enable propagation direction-dependent interactions between guided optical modes and circularly dichroic materials. Electrical tuning of interface chirality would aid active, switchable non-reciprocity in on-chip optoelectronic and photonic circuitry, but remains an outstanding challenge. Here, we report electrically controllable chirality in a nanophotonic interface with atomically thin monolayer tungsten diselenide (WSe_2). Titanium dioxide waveguides are directly fabricated on the surface of low-disorder, boron nitride-encapsulated WSe_2. Following integration, photoluminescence from excitonic states into the waveguide can be electrically switched between balanced and directionally biased emission. The operational principle leverages the doping-dependent valley polarization of excitonic states in WSe_2. Furthermore, the nanophotonic waveguide can function as a near-field source for diffusive exciton fluxes, which display valley and spin polarizations that are inherited from the interface chirality. Our versatile fabrication approach enables the deterministic integration of photonics with van der Waals heterostructures and could provide optical control over their excitonic and charge-carrier behaviour.

In tightly confined, propagating optical fields, Gauss's law requires that a rapidly varying electric field in the transverse direction must be accompanied by an electric field in the longitudinal direction that is 90° out of phase with the transverse field[1,2]. The transverse and longitudinal field components combine to create regions of elliptical polarization in which the transverse component of the optical spin angular momentum is locked to the direction of the wavevector of the optical mode. Notably, in such tightly confined fields, the optical spin angular momentum has a component perpendicular to the propagation direction, in contrast to paraxial circularly polarized free-space optical fields. This phenomenon, referred to as optical spin–orbit coupling (OSOC), has been observed in a variety of experimental platforms, including optical fibres[3–5], whispering gallery mode resonators[5–7], photonic crystal waveguides[8,9], plasmonic waveguides[10] and hyperbolic metamaterials[11] and metasurfaces[12].

Photonic structures exhibiting OSOC can be coupled with circularly dichroic materials—that is, materials that interact selectively with circularly polarized light—to generate chiral light–matter interfaces. Such interfaces create light–matter interactions that depend on the propagation direction of the light and provide a foundation for new photonic and plasmonic technologies, such as on-chip beam splitting for circularly polarized input light[13] and optically driven optical isolation[14]. Beyond classical systems, OSOC enables directional quantum nonlinear interactions between quantum states of photons and matter and has stimulated the development of chiral quantum optics[15].

An emerging platform for these chiral optical interfaces is atomically thin transition metal dichalcogenides (TMDCs). TMDC monolayers are direct bandgap semiconductors with optical resonances in the visible and near-infrared range dominated by excitonic states[16,17]. Owing to broken inversion symmetry in the monolayer crystal lattice, two inequivalent sets of bandgap minima exist at the momentum space K points (that is, K and K′ valleys), which couple to light of opposite circular polarization[18–21]. Preliminary demonstrations with plasmonic, nanowire and photonic crystal systems[10,22–27] have shown the feasibility of coupling light to TMDC valley excitonic states through OSOC. However, the scalable, deterministic incorporation of such architectures in existing integrated photonic platforms is challenging to achieve due to large propagation losses, restrictive design constraints and poor processing compatibility with delicate TMDC materials. Moreover, the chiral TMDC interfaces demonstrated so far are passive. A scalable nanophotonic–TMDC interface equipped with active electrical tunability could enable new applications in optoelectronic and integrated photonic technologies. Valley polarization, which characterizes the circular dichroism of TMDCs, can be modified via electrostatic doping[28], providing an avenue for active control. In addition, in monolayer TMDCs, in contrast to the multilayer TMDCs used previously[10], the exciton valley index determines the spin configurations of the underlying charge carriers in charged excitonic states[18]. Therefore, a photonic–TMDC interface also provides the opportunity to control semiconductor spins[29] with integrated photonics, enabling nanoscale optical manipulation of solid-state memories[30,31].

Results

Electrically controlled chiral interface. Here, we demonstrate an interface that exploits these unique material properties to realize electrically tunable chirality. The interface is based on deterministic fabrication of nanophotonic structures on arbitrary substrates and can be applied to a range of devices, facilitating broader application of chiral interfaces in nanophotonic circuitry. Our device consists of a titanium dioxide (TiO_2) nanophotonic waveguide fabricated on a WSe_2 monolayer that is encapsulated in hexagonal boron nitride (hBN) (Fig. 1a). Encapsulation with hBN substantially reduces inhomogeneity in TMDCs[32,33] and serves as a dielectric for electrostatic tuning[34]. Electrical control is achieved with a few-layer graphene (FLG) back gate and contact flakes (for fabrication details, see Methods). We fabricate TiO_2 waveguides on top of these heterostructures using templated atomic layer deposition[35].

[1]Pritzker School of Molecular Engineering, University of Chicago, Chicago, IL, USA. [2]Department of Physics, University of Chicago, Chicago, IL, USA. [3]Center for Molecular Engineering and Materials Science Division, Argonne National Laboratory, Lemont, IL, USA. [4]These authors contributed equally: Robert Shreiner, Kai Hao. ✉e-mail: ahigh@uchicago.edu

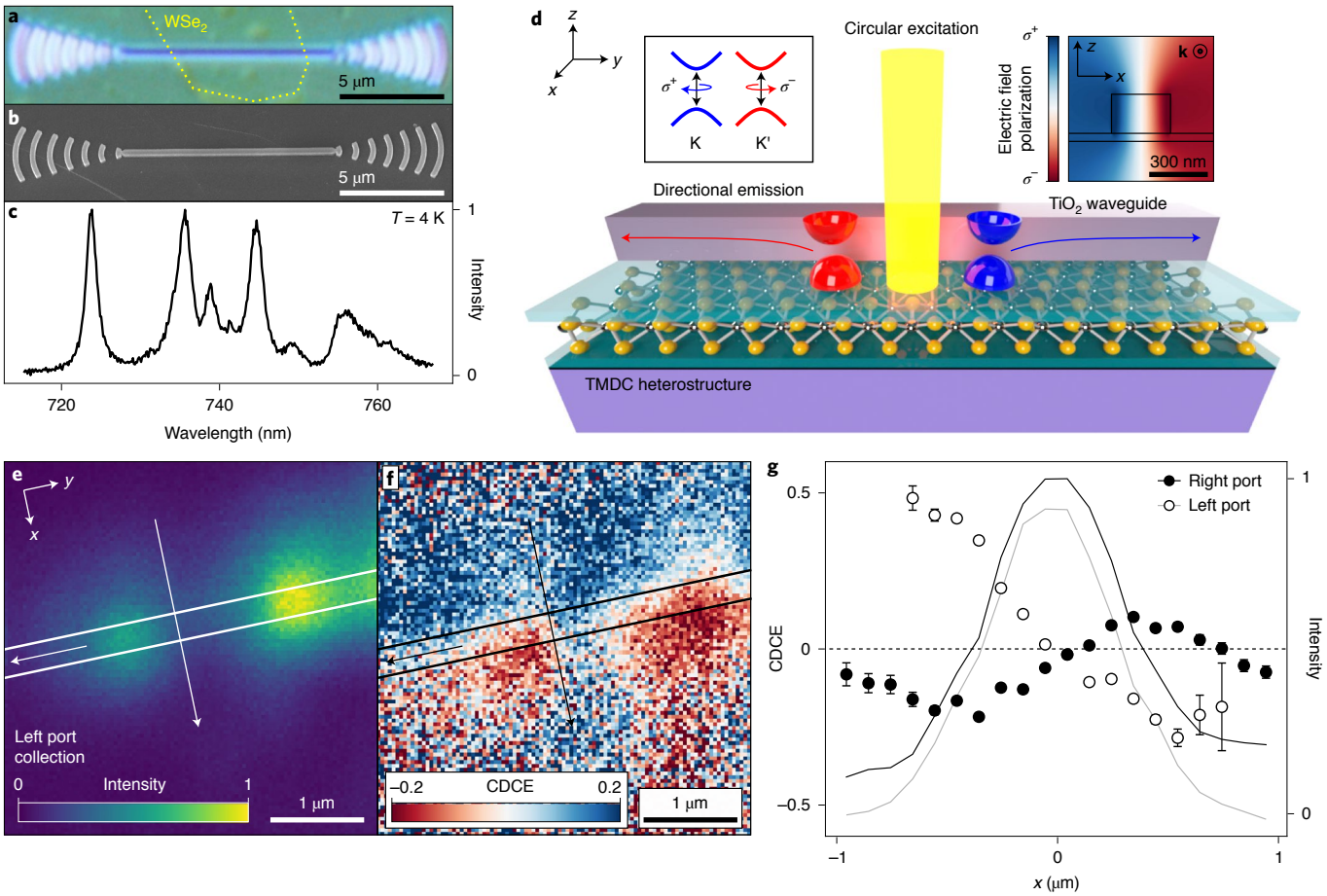

Fig. 1 | Chiral nanophotonic–TMDC interface. a,**b**, Optical (**a**) and scanning electron microscope (**b**) images representative of the TMDC–waveguide interface. The WSe_2 monolayer is marked by the yellow dotted line. **c**, PL spectrum of encapsulated WSe_2 at 4 K shows prominent exciton, trion and charged biexciton peaks. **d**, Schematic depicting chiral–directional coupling. Left inset: valley-dependent optical selection rules of monolayer TMDCs. Right inset: polarization of electric field distribution of waveguide mode with wavevector k propagating out of the page. **e**, Spatial mapping of PL intensity measured through the left port under linear far-field excitation. **f**, Spatial mapping of CDCE through the left port under circular far-field excitation. **g**, Line cuts of CDCE across the waveguide along the arrow direction in **e** and **f** for left (open circles) and right (filled circles) ports. Lines show the total intensity (that is, $I_{GP}{}^{\sigma+} + I_{GP}{}^{\sigma-}$) measured for each port. Data points are presented as mean values over the full spectral range with error bars corresponding to 1 s.d. of the background noise.

This fabrication method produces low-loss nanophotonic structures (Fig. 1b) without damaging the underlying substrate, making it ideal for interfacing with two-dimensional materials (for an image of the measured device, see Supplementary Fig. 1). Following waveguide fabrication, the WSe_2 monolayer exhibits narrow linewidth excitonic emission (Fig. 1c), confirming that our photonic integration process generates minimal inhomogeneities in the van der Waals heterostructure and is suitable for photonic integration with TMDCs.

Figure 1d illustrates the directional coupling that emerges between the waveguide modes and the TMDC material. The electric field distribution (for full simulation data, see Supplementary Section 2) of the propagating transverse electric mode is tightly confined (waveguide width $< \lambda/2$), manifesting in-plane, circularly polarized evanescent fields (Fig. 1d, right inset). The sign of the polarization, $\sigma+$ or $\sigma-$ (for definitions, see Supplementary Section 2), inverts across the waveguide and with the propagation direction. Depending on their location, excitons in the K and K′ valleys (Fig. 1d, left inset) will selectively couple to left- or right-wards propagating modes of the waveguide, thus establishing chiral–directional coupling at the waveguide–monolayer interface.

To characterize the interface, we first generate excitons and observe their radiative emission into the guided optical modes of the waveguide. The monolayer is excited from the far-field using a 660 nm laser with a spot size ~495 nm (see Supplementary Section 1). Excitonic photoluminescence (PL) couples to the waveguide and is detected via collecting the light scattered from gratings at the waveguide ends. Figure 1e displays the measured PL intensity from the left port (for the right port data, see Supplementary Fig. 9d) when a linearly polarized excitation is scanned around the waveguide. To study the chiral–directional coupling, we switch the polarization of the excitation laser from linear to circular, $\sigma+$ and $\sigma-$, creating valley-polarized excitonic states that preferably emit with the same polarization as the excitation (Fig. 1d). We characterize the interface using the chiral–directional coupling efficiency (CDCE). Here, $\mathrm{CDCE}(x,y) = [I_{GP}(x,y)^{\sigma+} - I_{GP}(x,y)^{\sigma-}]/[I_{GP}(x,y)^{\sigma+} + I_{GP}(x,y)^{\sigma-}]$, where $I_{GP}(x,y)^{\sigma+(\sigma-)}$ is the PL intensity measured from a specific grating port under $\sigma+(\sigma-)$ excitation at position (x,y). Figure 1f shows the spatial mapping of the CDCE for left port collection (for the right port data, see Supplementary Fig. 9e). As anticipated[10,25], we observe that the sign of the CDCE inverts as the excitation spot crosses the waveguide, approaching a magnitude of 20%, and that

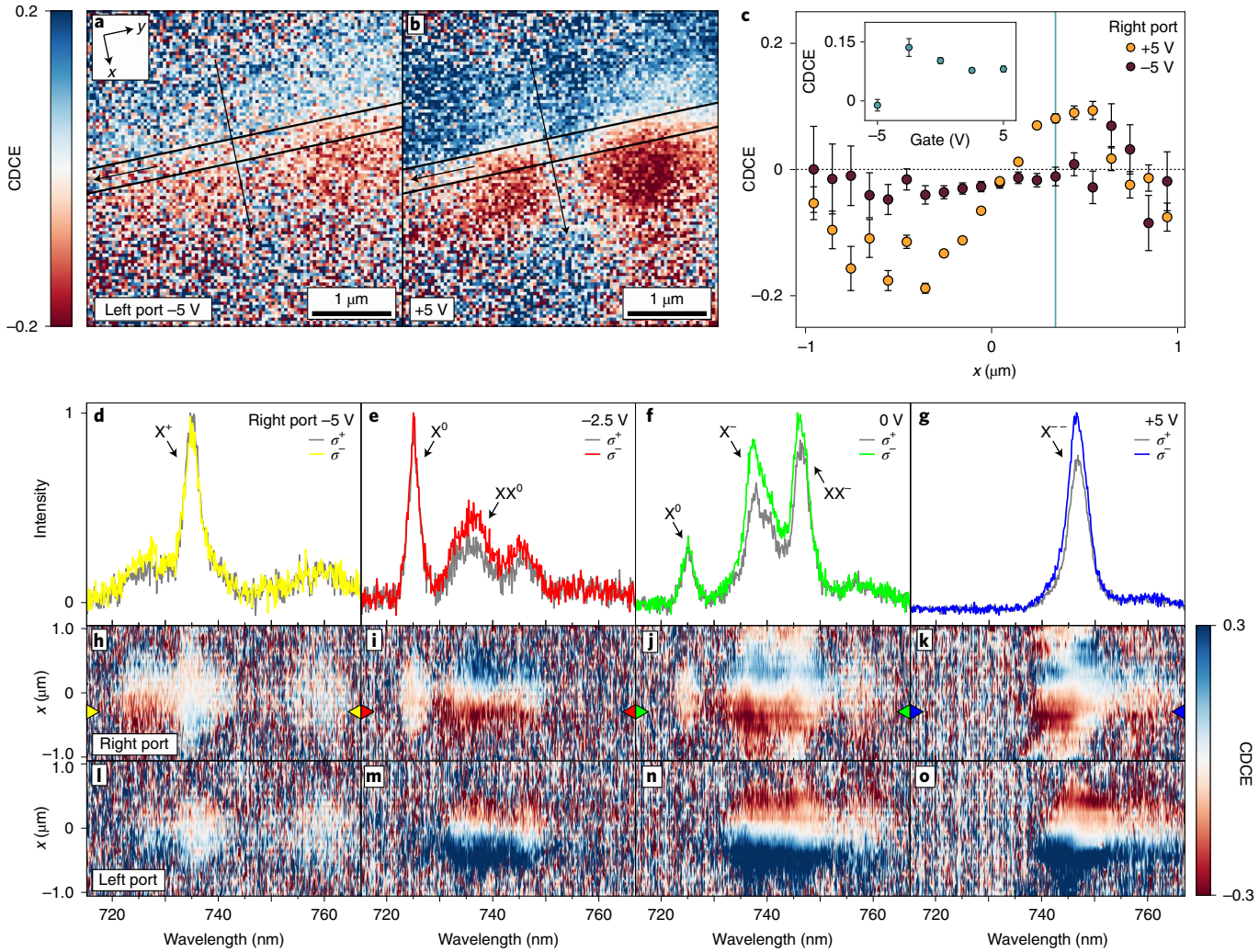

Fig. 2 | Electrostatic tuning of interface. a,**b**, Spatial mapping of CDCE of emission collected through the left port under an applied gate bias of −5 V (**a**) and 5 V (**b**). **c**, Line cuts of CDCE of emission collected through the right port along the arrow direction in **a** and **b**. Inset: gate dependence of CDCE at $x = +300$ nm (blue vertical line in the main plot). Data points are presented as mean values over the full spectral range with error bars corresponding to 1 s.d. of the background noise. **d**–**g**, PL out-coupled from the right port under a gate voltage of −5 V (**d**), −2.5 V (**e**), 0 V (**f**) and 5 V (**g**) with $\sigma+$ and $\sigma-$ excitations fixed at $x \approx -300$ nm. Excitonic states are labelled. **h**–**k** (**l**–**o**), Spectrally resolved spatial mapping of right (left) port CDCE at a gate voltage of −5 V (**h** (**l**)), −2.5 V (**i** (**m**)), 0 V (**j** (**n**)) and 5 V (**k** (**o**)). Coloured triangles in **h**–**k** indicate the corresponding spectral line cuts in **d**–**g**, respectively.

the sign of the CDCE flips between the two outcoupling ports (Fig. 1g). We also note that under linearly polarized excitation, the chiral–directional coupling vanishes as expected (see Supplementary Fig. 9c,f). For both ports, the CDCE goes to zero near the centre of the waveguide ($x = 0$ μm), where the mode polarization is linear (Fig. 1d, right inset). Far from the waveguide centre, the CDCE also falls to zero as the low signal-to-noise ratio dominates. These experimental signatures directly verify the predicted chiral interface between the TMDC monolayer and the photonic waveguide.

The integration of contacts and electrodes in our device architecture enables us to electrically dope the TMDC monolayer and, in turn, potentially control the chirality of our integrated photonic interface. To study this tunability, we apply a gate voltage to the TMDC monolayer and investigate the impact on the chiral–directional coupling. Figure 2a,b show the spatially mapped CDCE measured for gate voltages of −5 V and 5 V, respectively (for the right port data, see Supplementary Fig. 10d,f). The CDCE notably diminishes under negative applied bias. Comparing transverse line cuts across the waveguide (Fig. 2c), the CDCE spatial dependence at −5 V flattens to zero, whereas at +5 V it displays the expected crossing at $x = 0$ μm. At a fixed displacement of ~300 nm away from the waveguide, we observe a sharp transition in CDCE from near 0% at −5 V to around 15% at −2.5 V (Fig. 2c, inset). This result directly demonstrates the active electrical control over the chirality of the TMDC–waveguide interface.

To investigate the electrical tuning in more detail, we perform spectrally resolved measurements of the out-coupled PL. Figure 2d–g shows gate-dependent PL spectra collected from the right grating port for fixed-position off-waveguide $\sigma+$ and $\sigma-$ excitations. We attribute the characteristic peaks to the neutral and charged exciton and biexciton states delineated in recent literature reports[28,36,37]. Combining this spectroscopic information with the electrostatic control afforded by our high-quality interface, we analyse the chiral–directional coupling for each excitonic state. From the spectra in Fig. 2d–g, we find that the positive trion (X^+) and neutral exciton (X^0) states display balanced emission into the waveguide, independent of the excitation polarization. By contrast, the negative trion (X^- and X^{--}) and biexciton (XX^0 and XX^-) states exhibit directional emission. More completely, Fig. 2h–k(l–o) shows the wavelength-resolved right (left) port CDCE versus the position of

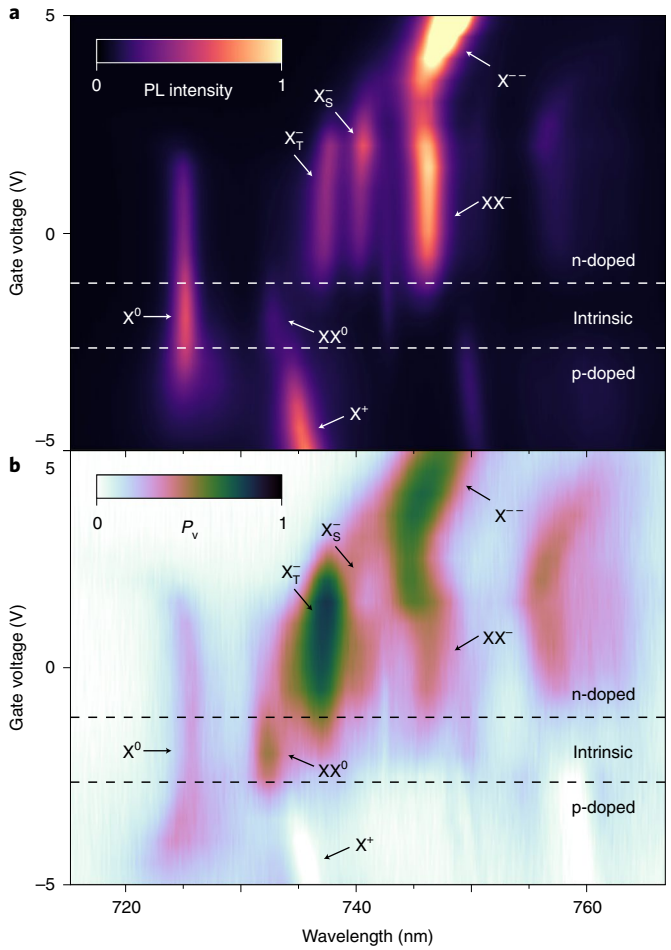

Fig. 3 | Gate dependence of valley polarization. a, Unpolarized PL spectra versus gate voltage under far-field excitation and collection. **b**, P_v of emission from electrostatically tuned excitonic states in WSe_2. In **a** and **b**, the relevant excitonic states are highlighted and the approximate doping regimes are labelled.

the excitation beam. Minimal variation is observed for the X^+ and X^0 peaks, whereas for the X^-, X^{--}, XX^0 and XX^- peaks, the CDCE inverts across the waveguide and reaches magnitudes near 20% on either side (for complete data, see Supplementary Fig. 11). These measurements indicate that the different excitonic states in the monolayer exhibit varying degrees of chiral–directional coupling and that the electrostatic control of this coupling correlates with switching between the dominant excitonic states.

To better understand the doping-dependent chiral–directional coupling for different excitonic states, we perform gated far-field PL measurements of the encapsulated WSe_2. Figure 3a shows the unpolarized PL versus the wavelength and gate voltage, which exhibits characteristic peaks for different doping regimes. Figure 3b plots the degree of circular polarization (DOCP), which characterizes the valley polarization P_v, defined as $P_v = [I_{co} - I_{cross}]/[I_{co} + I_{cross}]$, where $I_{co(cross)}$ refers to the PL intensity collected co(cross)-circularly polarized to the excitation. Importantly, the valley polarization results revealed here agree with the chiral–directional couplings of the respective excitonic states at the interface. Notably, X^+ shows no valley polarization, which explains the quenched waveguide coupling in the hole region, while X_T^- (triplet trion) and X^{--} show the strongest far-field polarization, as well as the clearest CDCE signatures. Considering these far-field valley polarization results, we fit the measured CDCE profiles for the excitonic states to simulations and find an isolated interface fidelity as high as $90 \pm 2\%$ (see Supplementary Section 2).

Our observation of widely differing valley polarizations for different species can be understood by considering valley relaxation processes that occur at differing rates. We consider two distinct processes that contribute to valley relaxation: the exchange interaction and the intervalley charge-carrier scattering. The exchange interaction is considered the primary depolarization mechanism for neutral excitons and negative trions[38,39]. The fast scattering of electron–hole pairs into the opposite valley depolarizes neutral excitons (Supplementary Fig. 16a). Through this same process, the K valley triplet trions rapidly relax to the energetically lower singlet trions (X_S^-) in the K′ valley, quickly eroding the polarization of existent singlet trions (Supplementary Fig. 16b). Inversely, the depolarization of triplet trions can result from exchange-interaction-induced intervalley scattering from energetically lower singlet trions (Supplementary Fig. 16c). However, this process is energetically unfavourable and, thus, highly suppressed, leaving triplet trions highly valley polarized. In addition to these exchange-interaction mechanisms, intervalley scattering of charge carriers also can lead to valley depolarization. For positive trions, the small spin splitting of the conduction band allows ready scattering of electrons into the opposite valley (Supplementary Fig. 16d), leading to fast depolarization[40]. For negative trions (triplet case in Supplementary Fig. 16e), the large valence band splitting suppresses the hole scattering in between the valleys. Such scattering processes, then, will not contribute substantially to the valley depolarization of negative trions. The measured results described by these depolarization pictures confirm that the tuning of the chirality in the photonic interface is due to gate modification of the valley dynamics in monolayer TMDCs.

Driving valley(spin)-polarized exciton fluxes. In addition to enabling electrical control over chiral–directional coupling of the excitonic emission, the TMDC–waveguide interface opens new possibilities to locally create and manipulate excitons and spins. With improvements in sample quality and the observation of long-lived excitons in heterostructures, exciton diffusion in two-dimensional semiconductors has recently garnered increasing interest, providing a context for the fundamental exploration of planar spatial dynamics in systems with many-particle interactions[41,42] and enabling optoelectronic technologies such as room-temperature excitonic transistors[43]. Unlike in bare, few-layer samples[26], the encapsulated TMDC monolayers in our interface provide reduced-disorder environments for studying exciton propagation[44] and preserve spin-valley locking, enabling the simultaneous transport of spin-polarized charge carriers. Compared with the far-field optical excitations currently utilized to drive exciton diffusion, the waveguide modes of high-index nanophotonic structures can act as compact, tailored, on-chip sources of exciton fluxes. Moreover, the high DOCP of their evanescent fields enables the generation of valley-polarized exciton fluxes[45–47], which can be directionally reconfigured (Fig. 4a). Therefore, a new modality for injecting spin currents in semiconductors with integrated photonics—in contrast to the case with conventional ferroelectric contacts[48,49]—can be realized, promising advancements in optical computing and spintronics[50].

With our device, we first show that the waveguide can locally generate diffusive excitons. To probe this functionality, we couple the excitation laser into the right grating port and collect the PL emitted from the TMDC monolayer into the far-field. Figure 4b shows the spatial distribution of the exciton PL spectrally selected over the wavelength regions of interest (for representative spectra with peak identifications, see Supplementary Fig. 14). The shaded area illustrates the simulated electric field intensity of the waveguide mode. The quickly decaying evanescent tail implies a large density gradient of the excitonic states generated by the mode, which induces

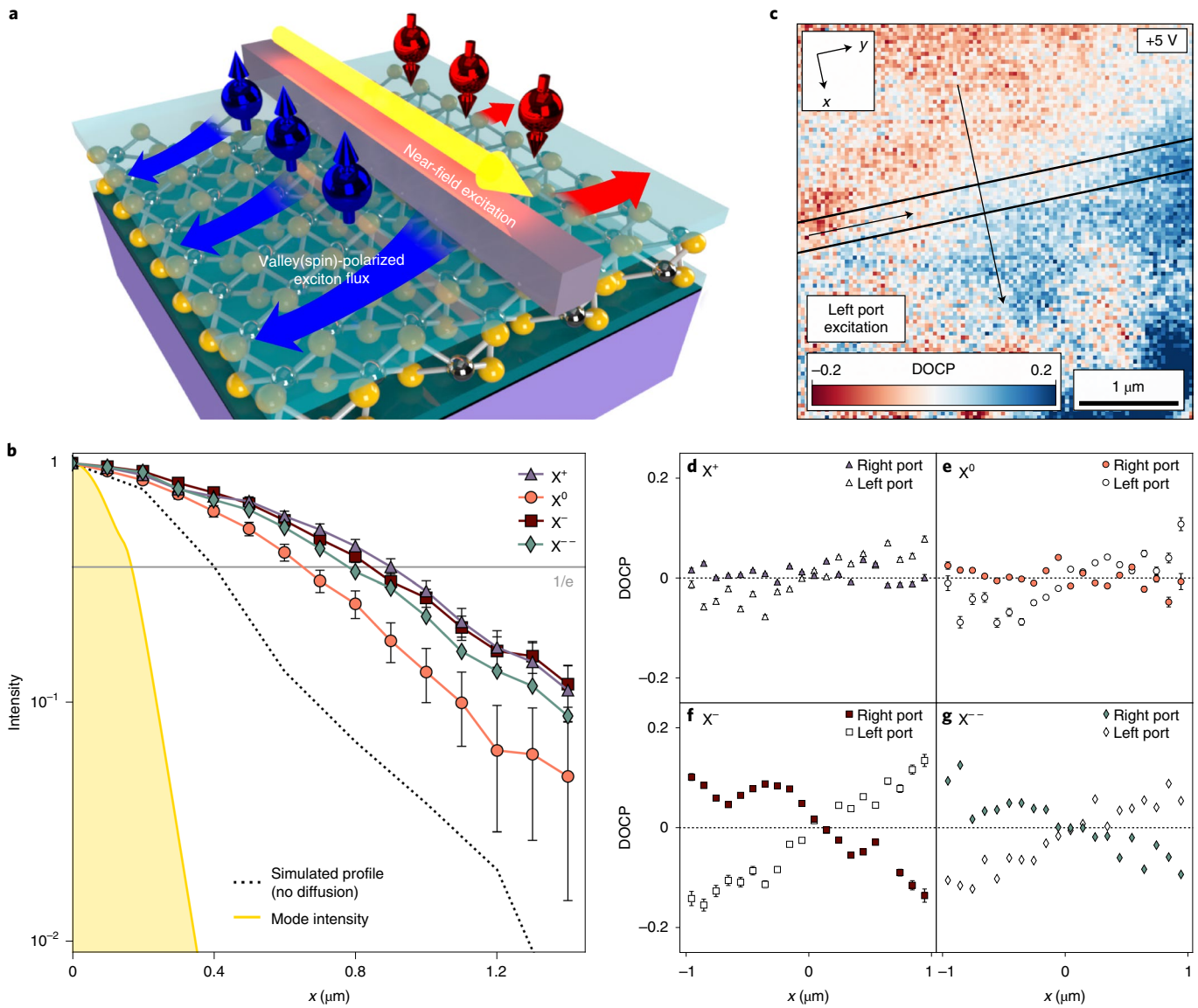

Fig. 4 | Photonic pumping of valley(spin)-polarized exciton fluxes. a, Schematic of valley(spin)-polarized exciton flux generation. Outward-pointing arrows (blue/red) indicate the diffusion of oppositely valley-polarized excitons carrying spins for the fixed propagation direction of the waveguide excitation mode (yellow). **b**, Normalized PL intensity distributions versus distance from waveguide (centre at $x = 0\,\mu m$) for different excitonic states. The shaded area is the simulated electric field intensity profile of the guided mode in the waveguide. The dotted line shows the simulated collection profile in the absence of diffusion given the experimental resolution. **c**, DOCP map under 5 V gate bias, left port excitation, and far-field collection. **d**–**g**, DOCP of excitonic states X^+ (**d**), X^0 (**e**), X^- (**f**) and X^{--} (**g**) along the arrow direction in **c**. Open (filled) symbols correspond to rightward (leftward) propagating waveguide excitation in-coupled through the left (right) grating port. In **b** and **d**, data points are presented as mean values over the respective spectral ranges with error bars corresponding to 1 s.d. of the background noise.

their diffusive transport away from the waveguide. Considering the measured resolution of our collection channel (see Supplementary Section 1), we compute the anticipated PL spatial distribution in the absence of exciton diffusion (dotted line in Fig. 4b; for simulation information see Supplementary Section 2). We find that the profiles of the excitonic states extend beyond this boundary, indicating their diffusion away from the waveguide. For the charged excitons, both negative and positive, we extract the 1/e diffusion lengths $L_{X\pm} \approx 0.45\,\mu m$ based on the predicted no-diffusion profile. The neutral exciton displays a diffusion length $L_{X^0} \approx 0.25\,\mu m$. These diffusion lengths of hundreds of nanometres are comparable to literature values[51]. The excellent sample quality and comprehensive electrostatic control over our interface enable this extraction of state-specific diffusion.

We next examine the valley(spin)-polarization of these near-field-driven exciton fluxes. As before, the evanescent fields on either side of the waveguide exhibit opposite nearly circular polarizations and therefore populate the excitonic states in opposite valleys (Fig. 4a). To measure this resulting valley polarization, we analyse the circular polarization of the far-field PL. The valley polarization of the excitonic states is characterized by the PL DOCP. Here, $DOCP(x,y) = [I_{FF}(x,y)^{\sigma+} - I_{FF}(x,y)^{\sigma-}]/[I_{FF}(x,y)^{\sigma+} + I_{FF}(x,y)^{\sigma-}]$, where $I_{FF}(x,y)^{\sigma+(\sigma-)}$ is the $\sigma+(\sigma-)$ component of the far-field PL intensity collected at position (x,y). Figure 4c shows the DOCP measured under left port excitation and 5 V gate bias, confirming the generation of valley-polarized excitonic states (for additional port and gate voltage results, see Supplementary Figs. 12 and 13). Figure 4d–g displays the position-dependent, spectrally resolved DOCP for the

respective X^+, X^0, X^- and X^{--} peaks, respectively. Like the CDCE (Fig. 2d–g) and far-field P_v (Fig. 3b) results, negative trions exhibit a large DOCP, whereas positive trions and neutral excitons show nearly zero DOCP. We also note the presence of prominent dark trion peaks at ~750 nm (ref. [52]) (Supplementary Fig. 14). Owing to their linear out-of-plane dipole moment[34], dark trions predominantly couple to the transverse magnetic mode, showing biased DOCP with a spatial profile that is independent of the excitation port. For negative trions, owing to valley–spin locking, the paired hole spin is fixed by the valley index (see Supplementary Section 5). Thus, spin-polarized holes are injected with the valley-polarized X^- and X^{--} states. With the diffusion measurements described above, we conclude that our chiral photonic interface serves as a directionally reconfigurable source for injecting hole spin currents in atomically thin semiconductors.

Discussion

We have demonstrated a photonic waveguide interfaced with an hBN-encapsulated, electrically gated WSe_2 monolayer. The interface exhibits a CDCE that is electrically tunable from 0% to 20% and generates valley(spin)-polarized exciton fluxes via near-field excitation. Beyond linear waveguides, our versatile nanophotonic fabrication method can interface TMDCs with more complicated photonic structures where device geometry and size are limited only by the constraints of advanced lithography[35], enabling photonic ring modulators and inteferometers[53] and exciton–polaritons in photonic crystals[27]. Combined with recent advances in large-area growth[54], exfoliation[55,56] and assembly[57] of two-dimensional materials, which will improve heterostructure yield and scalability beyond current limitations, this work establishes a universal platform for their deterministic, wafer-scale integration with nanophotonic circuitry. Importantly, this interface's tunable chirality, previously unavailable in other chiral optical interfaces, relies on the doping-dependent valley dynamics of exciton states in the TMDC monolayer. Multilayer and twisted van der Waals heterostructures display engineered, exotic valley properties[58–60] that can also be combined with this waveguide interface for additional chiral functionalities, such as gate-reversible emission routing[61], and offering new photonic logic and control schemes based on two-dimensional materials. In addition, nanophotonic driving of exciton diffusion in atomically thin semiconductors creates a bridge between distributed photonic elements and local excitonic circuits[62–64]. Moreover, near-field optical pumping through chiral TMDC–photonic interfaces can be used to generate the spin polarization of resident charge carriers in monolayers[65–67]. Such optically prepared spin-polarized electronic states, which are sensitive to the carrier doping level, can break the time-reversal symmetry of the interface, enabling gate-activated all-optical non-reciprocity in integrated nanophotonic architectures[68].

Online content

Any methods, additional references, Nature Research reporting summaries, source data, extended data, supplementary information, acknowledgements, peer review information; details of author contributions and competing interests; and statements of data and code availability are available at https://doi.org/10.1038/s41566-022-00971-7.

Received: 9 August 2021; Accepted: 3 February 2022;
Published online: 17 March 2022

References

1. Aiello, A., Banzer, P., Neugebaueru, M. & Leuchs, G. From transverse angular momentum to photonic wheels. *Nat. Photonics* **9**, 789–795 (2015).
2. Bliokh, K. Y., Rodriguez-Fortuno, F. J., Nori, F. & Zayats, A. V. Spin–orbit interactions of light. *Nat. Photonics* **9**, 796–808 (2015).
3. Petersen, J., Volz, J. & Rauschenbeutel, A. Chiral nanophotonic waveguide interface based on spin–orbit interaction of light. *Science* **346**, 67–71 (2014).
4. Mitsch, R., Sayrin, C., Albrecht, B., Schneeweiss, P. & Rauschenbeutel, A. Quantum state-controlled directional spontaneous emission of photons into a nanophotonic waveguide. *Nat. Commun.* **5**, 5713 (2014).
5. Sayrin, C. et al. Nanophotonic optical isolator controlled by the internal state of cold atoms. *Phys. Rev. X* **5**, 041036 (2015).
6. Shomroni, I. et al. All-optical routing of single photons by a one-atom switch controlled by a single photon. *Science* **345**, 903–906 (2014).
7. Scheucher, M., Hilico, A., Will, E., Volz, J. & Rauschenbeutel, A. Quantum optical circulator controlled by a single chirally coupled atom. *Science* **354**, 1577–1580 (2016).
8. le Feber, B., Rotenberg, N. & Kuipers, L. Nanophotonic control of circular dipole emission. *Nat. Commun.* **6**, 6695 (2015).
9. Soellner, I. et al. Deterministic photon–emitter coupling in chiral photonic circuits. *Nat. Nanotechnol.* **10**, 775–778 (2015).
10. Gong, S. H., Alpeggiani, F., Sciacca, B., Garnett, E. C. & Kuipers, L. Nanoscale chiral valley–photon interface through optical spin–orbit coupling. *Science* **359**, 443–447 (2018).
11. Kapitanova, P. V. et al. Photonic spin Hall effect in hyperbolic metamaterials for polarization-controlled routing of subwavelength modes. *Nat. Commun.* **5**, 3226 (2014).
12. High, A. A. et al. Visible-frequency hyperbolic metasurface. *Nature* **522**, 192–196 (2015).
13. Lin, J. et al. Polarization-controlled tunable directional coupling of surface plasmon polaritons. *Science* **340**, 331–334 (2013).
14. Tang, L. et al. On-chip chiral single-photon interface: isolation and unidirectional emission. *Phys. Rev. A* **99**, 43833 (2019).
15. Lodahl, P. et al. Chiral quantum optics. *Nature* **541**, 473–480 (2017).
16. Mak, K. F., Lee, C., Hone, J., Shan, J. & Heinz, T. F. Atomically thin MoS_2: a new direct-gap semiconductor. *Phys. Rev. Lett.* **105**, 136805 (2010).
17. Splendiani, A. et al. Emerging photoluminescence in monolayer MoS_2. *Nano Lett.* **10**, 1271–1275 (2010).
18. Xiao, D., Liu, G. B., Feng, W. X., Xu, X. D. & Yao, W. Coupled spin and valley physics in monolayers of MoS_2 and other group-VI dichalcogenides. *Phys. Rev. Lett.* **108**, 196802 (2012).
19. Zeng, H., Dai, J., Yao, W., Xiao, D. & Cui, X. Valley polarization in MoS_2 monolayers by optical pumping. *Nat. Nanotechnol.* **7**, 490–493 (2012).
20. Mak, K. F., He, K., Shan, J. & Heinz, T. F. Control of valley polarization in monolayer MoS_2 by optical helicity. *Nat. Nanotechnol.* **7**, 494–498 (2012).
21. Cao, T. et al. Valley-selective circular dichroism of monolayer molybdenum disulphide. *Nat. Commun.* **3**, 887 (2012).
22. Chervy, T. et al. Room temperature chiral coupling of valley excitons with spin-momentum locked surface plasmons. *ACS Photonics* **5**, 1281–1287 (2018).
23. Sun, L. Y. et al. Separation of valley excitons in a MoS_2 monolayer using a subwavelength asymmetric groove array. *Nat. Photonics* **13**, 180–184 (2019).
24. Yang, Z. L., Aghaeimeibodi, S. & Waks, E. Chiral light–matter interactions using spin-valley states in transition metal dichalcogenides. *Opt. Express* **27**, 21367–21379 (2019).
25. Guo, Q. B. et al. Routing a chiral Raman signal based on spin–orbit interaction of light. *Phys. Rev. Lett.* **123**, 183903 (2019).
26. Gong, S. H., Komen, I., Alpeggiani, F. & Kuipers, L. Nanoscale optical addressing of valley pseudospins through transverse optical spin. *Nano Lett.* **20**, 4410–4415 (2020).
27. Liu, W. J. et al. Generation of helical topological exciton–polaritons. *Science* **370**, 600–604 (2020).
28. Barbone, M. et al. Charge-tuneable biexciton complexes in monolayer WSe_2. *Nat. Commun.* **9**, 3721 (2018).
29. Dey, P. et al. Gate-controlled spin-valley locking of resident carriers in WSe_2 monolayers. *Phys. Rev. Lett.* **119**, 137401 (2017).
30. Rice, W. D. et al. Persistent optically induced magnetism in oxygen-deficient strontium titanate. *Nat. Mater.* **13**, 481–487 (2014).
31. Lalieu, M. L. M., Lavrijsen, R. & Koopmans, B. Integrating all-optical switching with spintronics. *Nat. Commun.* **10**, 110 (2019).
32. Cadiz, F. et al. Excitonic linewidth approaching the homogeneous limit in MoS_2-based van der Waals heterostructures. *Phys. Rev. X* **7**, 21026 (2017).
33. Ajayi, O. A. et al. Approaching the intrinsic photoluminescence linewidth in transition metal dichalcogenide monolayers. *2d Mater.* **4**, 31011 (2017).
34. Zhou, Y. et al. Probing dark excitons in atomically thin semiconductors via near-field coupling to surface plasmon polaritons. *Nat. Nanotechnol.* **12**, 856–860 (2017).
35. Butcher, A. et al. High-Q nanophotonic resonators on diamond membranes using templated atomic layer deposition of TiO_2. *Nano Lett.* **20**, 4603–4609 (2020).
36. Ye, Z. L. et al. Efficient generation of neutral and charged biexcitons in encapsulated WSe_2 monolayers. *Nat. Commun.* **9**, 3718 (2018).
37. Li, Z. P. et al. Revealing the biexciton and trion-exciton complexes in BN encapsulated WSe_2. *Nat. Commun.* **9**, 3719 (2018).

38. Yu, T. & Wu, M. W. Valley depolarization due to intervalley and intravalley electron–hole exchange interactions in monolayer MoS_2. *Phys. Rev. B* **89**, 205303 (2014).
39. Singh, A. et al. Long-lived valley polarization of intravalley trions in monolayer WSe_2. *Phys. Rev. Lett.* **117**, 257402 (2016).
40. Scuri, G. et al. Electrically tunable valley dynamics in twisted WSe_2/WSe_2 bilayers. *Phys. Rev. Lett.* **124**, 217403 (2020).
41. Kulig, M. et al. Exciton diffusion and halo effects in monolayer semiconductors. *Phys. Rev. Lett.* **120**, 207401 (2018).
42. Glazov, M. M. Quantum interference effect on exciton transport in monolayer semiconductors. *Phys. Rev. Lett.* **124**, 166802 (2020).
43. Unuchek, D. et al. Room-temperature electrical control of exciton flux in a van der Waals heterostructure. *Nature* **560**, 340–344 (2018).
44. Zipfel, J. et al. Exciton diffusion in monolayer semiconductors with suppressed disorder. *Phys. Rev. B* **101**, 115430 (2020).
45. Rivera, P. et al. Valley-polarized exciton dynamics in a 2D semiconductor heterostructure. *Science* **351**, 688–691 (2016).
46. Jin, C. H. et al. Imaging of pure spin-valley diffusion current in WS_2–WSe_2 heterostructures. *Science* **360**, 893–896 (2018).
47. Unuchek, D. et al. Valley-polarized exciton currents in a van der Waals heterostructure. *Nat. Nanotechnol.* **14**, 1104–1109 (2019).
48. Costache, M. V., Sladkov, M., Watts, S. M., van der Wal, C. H. & van Wees, B. J. Electrical detection of spin pumping due to the precessing magnetization of a single ferromagnet. *Phys. Rev. Lett.* **97**, 216603 (2006).
49. Sanchez, O. L., Ovchinnikov, D., Misra, S., Allain, A. & Kis, A. Valley polarization by spin injection in a light-emitting van der Waals heterojunction. *Nano Lett.* **16**, 5792–5797 (2016).
50. Zutic, I., Fabian, J. & Das Sarma, S. Spintronics: fundamentals and applications. *Revi. Mod. Phys.* **76**, 323–410 (2004).
51. Cadiz, F. et al. Exciton diffusion in WSe_2 monolayers embedded in a van der Waals heterostructure. *Appl. Phys. Lett.* **112**, 152106 (2018).
52. Liu, E. et al. Gate tunable dark trions in monolayer WSe_2. *Phys. Rev. Lett.* **123**, 027401 (2019).
53. Datta, I. et al. Low-loss composite photonic platform based on 2D semiconductor monolayers. *Nat. Photonics* **14**, 256–262 (2020).
54. Seol, M. et al. High-throughput growth of wafer-scale monolayer transition metal dichalcogenide via vertical Ostwald ripening. *Adv. Mater.* **32**, 2003542 (2020).
55. Liu, F. et al. Disassembling 2D van der Waals crystals into macroscopic monolayers and reassembling into artificial lattices. *Science* **367**, 903–906 (2020).
56. Huang, Y. et al. Universal mechanical exfoliation of large-area 2D crystals. *Nat. Commun.* **11**, 2453 (2020).
57. Mannix, A. J. et al. Robotic four-dimensional pixel assembly of van der Waals Solids. *Nat. Nanotechnol.* https://doi.org/10.1038/s41565-021-01061-5 (2022).
58. Seyler, K. L. et al. Signatures of moire-trapped valley excitons in $MoSe_2/WSe_2$ heterobilayers. *Nature* **567**, 66–70 (2019).
59. Tran, K. et al. Evidence for moire excitons in van der Waals heterostructures. *Nature* **567**, 71–75 (2019).
60. Jin, C. H. et al. Observation of moire excitons in WSe_2/WS_2 heterostructure superlattices. *Nature* **567**, 76–80 (2019).
61. Ciarrocchi, A. et al. Polarization switching and electrical control of interlayer excitons in two-dimensional van der Waals heterostructures. *Nat. Photonics* **13**, 131–136 (2019).
62. High, A. A., Novitskaya, E. E., Butov, L. V., Hanson, M. & Gossard, A. C. Control of exciton fluxes in an excitonic integrated circuit. *Science* **321**, 229–231 (2008).
63. Jauregui, L. A. et al. Electrical control of interlayer exciton dynamics in atomically thin heterostructures. *Science* **366**, 870–875 (2019).
64. Liu, Y. et al. Electrically controllable router of interlayer excitons. *Sci. Adv.* https://doi.org/10.1126/sciadv.aba1830 (2020).
65. Li, J. et al. Valley relaxation of resident electrons and holes in a monolayer semiconductor: dependence on carrier density and the role of substrate-induced disorder. *Phys. Rev. Mater.* **5**, 044001 (2021).
66. Robert, C. et al. Spin/valley pumping of resident electrons in WSe_2 and WS_2 monolayers. *Nat. Commun.* **12**, 5455 (2021).
67. Hao, K., Shreiner, R., & High, A. A. Optically controllable magnetism in atomically thin semiconductors. Preprint at https://arxiv.org/abs/2108.05931 (2021).
68. Guddala, S. et al. All-optical nonreciprocity due to valley polarization pumping in transition metal dichalcogenides. *Nat. Commun.* **12**, 3746 (2021).

Methods

Monolayer WSe_2 was mechanically exfoliated from bulk crystal (2D Semiconductors) onto (silicon dioxide/silicon) SiO_2/Si substrates with a 285 nm oxide thickness. The FLG and thin hBN flakes were similarly exfoliated from bulk materials (HQ Graphene). Optical contrast and atomic force microscopy were used to verify that each flake was smooth and of the appropriate thickness. After exfoliation, the hBN flakes were annealed in an inert argon atmosphere at 350 °C for 30 min to release any strain and remove tape residue.

Flakes were assembled into the gated monolayer WSe_2 heterostructure via a dry-transfer technique[69]. Using a stamp of polycarbonate (PC) film on polydimethylsiloxane, the top hBN layer (11 nm thick), the FLG contact gate, monolayer WSe_2, and bottom hBN layer (17 nm thick) were picked up in sequence. The PC film with the heterostructure then was stamped onto the exfoliated FLG back gate on the SiO_2/Si substrate. The PC film was dissolved in chloroform for 15 min at room temperature, leaving the bare heterostructure.

Titanium/gold contacts were patterned on the exposed FLG flakes using photolithography and deposited via electron beam evaporation (5 nm/95 nm, respectively). Subsequently, a 10 nm encapsulation layer of aluminium oxide was deposited via electron beam evaporation to protect the heterostructure and ensure a uniform surface for the photonics fabrication. The waveguide and grating couplers were patterned on top of the heterostructure using electron beam lithography[35]. A conformal TiO_2 layer was grown via atomic layer deposition into the device template. After etching the excess TiO_2 and stripping the poly(methyl methacrylate) (PMMA) template with *N*-methylpyrrolidone (NMP) (with heating to 80 °C and soaking the sample overnight), the TiO_2 waveguide was left on top of the heterostructure. The sample was then annealed in the ambient atmosphere at 250 °C for 2 h. Finally, a layer of PMMA (1.4 µm thick) was spin-coated onto the chip. The presented data were collected from the device shown in Supplementary Fig. 1. Measurements on an additional sample yielded consistent results.

Data availability

The data that support the findings of this study are available from the corresponding author upon reasonable request.

Code availability

The code used in this study is available from the corresponding author upon reasonable request.

References

69. Zomer, P. J., Guimarães, M. H. D., Brant, J. C., Tombros, N. & van Wees, B. J. Fast pick up technique for high quality heterostructures of bilayer graphene and hexagonal boron nitride. *Appl. Phys. Lett.* **105**, 13101 (2014).

Acknowledgements

This work made use of the Pritzker Nanofabrication Facility part of the Pritzker School of Molecular Engineering at the University of Chicago, which receives support from Soft and Hybrid Nanotechnology Experimental (SHyNE) Resource (NSF ECCS-2025633), a node of the National Science Foundation's National Nanotechnology Coordinated Infrastructure. This work also made use of the shared facilities at the University of Chicago Materials Research Science and Engineering Center, supported by the National Science Foundation under award number DMR-2011854. Funding was provided by Army Research Office Grant #W911NF-20-1-0217 (R.S. and K.H.) and the Boeing company (A.B.). A.B. acknowledges support from the NSF Graduate Research Fellowship under grant no. DGE-1746045. We acknowledge Y. Zhou, J. Park and A. Dibos for helpful discussions.

Author contributions

A.A.H. conceived the study. K.H., R.S. and A.B. developed the fabrication procedure. K.H. and R.S. performed experiments, analyses, and simulations. K.H., R.S. and A.A.H. wrote the manuscript with extensive input from all authors.

Competing interests

The authors declare no competing interests.

Additional information

Supplementary information The online version contains supplementary material available at https://doi.org/10.1038/s41566-022-00971-7.

Correspondence and requests for materials should be addressed to Alexander A. High.

Peer review information *Nature Photonics* thanks Mikhail Kats and the other, anonymous, reviewer(s) for their contribution to the peer review of this work.

Reprints and permissions information is available at www.nature.com/reprints.